Navigation of superparamagnetic particles with a pre-magnetized high-temperature superconducting bulk in a weak background field

OPEN ACCESS
IOP Publishing
Superconductor Science and Technology
Supercond. Sci. Technol. **37** (2024) 115008 (12pp)
https://doi.org/10.1088/1361-6668/ad7c8c

Navigation of superparamagnetic particles with a pre-magnetized high-temperature superconducting bulk in a weak background field

Alexandre Arsenault[1,3,*], **Frédéric Sirois**[1], **Ning Li**[2] and **Gilles Soulez**[2]

[1] Polytechnique Montréal, Montréal, QC H3C 3A7, Canada
[2] Centre de Recherche du Centre Hospitalier de l'Université de Montréal (CRCHUM), Montréal, QC H2X 0A9, Canada

E-mail: alexandre.arsenault94@gmail.com

Received 14 June 2024, revised 30 August 2024
Accepted for publication 18 September 2024
Published 1 October 2024

Abstract

Recent research has shown significant progress towards a full body magnetic drug delivery (MDD) system for use in targeted cancer treatments. Although many different MDD systems have been proposed to generate strong remote forces capable of rapidly changing directions at distances greater than 10 cm, current state-of-the-art technologies lack in force strength and/or degrees of freedom. Knowing that high temperature superconducting (HTS) bulks can achieve trapped fields an order of magnitude larger than ferromagnets, this work aims at numerically and experimentally evaluating the forces that can be produced by HTS bulks in a uniform magnetic field. We first use Hall probe measurements and finite element simulations to determine the magnetic field generated by an HTS pellet and show that both results are in good agreement. Using a combination of simulations and experiments, we then show that for a 14×6 mm $YBa_2Cu_3O_{7-x}$ pellet magnetized at 2 T, remote forces on superparamagnetic microparticles are maximized at background fields of $\sim$50 mT. In addition, the direction of the magnetic forces can be flipped by changing the direction of the applied field relative to the HTS's magnetization. The HTS bulk was successfully used to navigate magnetic microparticles in a glass bifurcation mimicking the hepatic artery of the human liver. Finally, we show by simulation that a large HTS pellet magnetized at 5 T in a field of $\sim$250 mT can generate stronger forces with more degrees of freedom than the strongest forces achievable in current MDD technologies.

Keywords: magnetic drug delivery, remote magnetic force, HTS magnetization, finite element method

[3] Alexandre Arsenault is now with the Paul Scherrer Institut, 5232 Villigen, Switzerland.
[*] Author to whom any correspondence should be addressed.

1. Introduction

Chemotherapy, one of the most commonly prescribed cancer treatments, consists of injecting cytotoxic drugs near the cancerous tumor to kill fast-growing cells. However, the systemic injection of these drugs leads to unwanted side effects due to healthy cells being affected by collateral damage. Indeed, only about 2% of the chemotherapeutic treatment affects cancerous cells [1, 2]. A promising technique to reduce side effects and improve treatment efficiency involves navigating the drugs directly to the tumor. Several methods have been proposed to achieve this by using magnetic fields [3], ultrasonic waves [4], and the enhanced permeability and retention effect [5]. The former has gained significant traction in recent years, with an emerging company expecting to do their first human clinical trials in early 2023 [6]. In this technology, dubbed magnetic drug delivery (MDD), the chemotherapeutic drugs are attached to magnetic nanoparticles or bacteria and steered towards the cancer with appropriate external magnetic fields.

Many challenges arise when remotely navigating particles in the human body due to constraints on the size, magnetic response and composition of the particles, leading to weak magnetic forces at appreciable distances. Three main criteria are required for a safe and successful navigation. First, the magnetic nanoparticles must be smaller than $\sim$100 nm in diameter to prevent embolization in smaller capillaries during their evacuation out of the patient [7]. In addition, they must be superparamagnetic so that they do not agglomerate in the absence of a magnetic field after the treatment is over [8]. Finally, the particles must be bio-compatible, meaning that materials with a strong magnetic response such as FeCo have limited use due to their biological toxicity [9]. The most commonly used particles in the literature are therefore made of Fe_3O_4 due to their relatively strong magnetization and extensive use in other biomedical applications [10–12]. Several magnetic nanoparticles can be embedded in a biodegradable matrix such as poly lactic-co-glycolic acid (PLGA) together with chemotherapeutic drugs to produce a magnetic microsphere (MMS) used for the navigation [9].

An ideal MDD system requires strong magnetic fields and field gradients to generate adequate remote forces at a distance, fast directional changes of the remote forces and a method for evaluating the navigation efficiency. Numerous techniques have been proposed to satisfy these requirements over the years. The simplest methods consist of using the magnetic fields generated by a permanent magnet (PM) or high temperature superconducting (HTS) pellet [13–16]. While the cost of this approach is very low, only attractive forces can be achieved and the range of the forces is low due to the rapidly decreasing magnetic field from the surface of the PM/HTS. Hence, deep tissue navigation at distances of $\sim$10 cm from the surface of the patient is impossible with this method.

More recently, the use of magnetic resonance imaging (MRI) scanners has shown significant promise for generating remote forces suitable for deep tissue navigation [17–21]. The strong uniform field of the MRI is more than sufficient to magnetically saturate the MMSs, while the imaging coils can be used for both the navigation and imaging of the MMSs [22]. Nonetheless, the magnetic field gradients produced by the imaging coils is limited to $\sim$40 mT m^{-1} in order to avoid overheating, thereby restricting the navigation efficiency. This issue can be circumvented by reducing the blood flow using a balloon catheter and by orienting the patient such that the gravitational force facilitates the navigation [23], but this leads to longer treatment times. Nevertheless, this method recently managed to navigate MMSs in large animal livers, demonstrating the possibility of human-scale treatments [24].

So far, the MDD candidate capable of generating the strongest remote forces is dipole field navigation (DFN) [25–28]. In this method, ferromagnetic (FM) cores are inserted into the uniform field of an MRI scanner to distort the field and generate appropriate field gradients. The position of each core must be carefully determined for multi-bifurcation navigation, which is done by using complex algorithms [29]. Although gradients stronger than 300 mT m^{-1} are achievable, the magnetic field distortion generated by the FM cores has limited reach. The remote forces obtained with this method are therefore limited for multiple bifurcations requiring rapid changes in field gradients [26].

Recently, we studied two methods of magnetic force generation combining MRI scanners and HTS bulks for MDD purposes by simulations [30]. The first method consists of inserting a zero-field cooled (ZFC) HTS pellet in the 3 T uniform field of an MRI, while the second method consists of magnetizing a field cooled (FC) HTS pellet by rotating it in the 1.5 T uniform field of an MRI. Although complementary or stronger forces than DFN can be obtained with these methods, the high background field produced by MRI scanners leads to large insertion forces and/or torque needed to magnetize the bulks.

In this work, we explore the use of HTS bulks for generating strong remote forces and fast directional changes on superparamagnetic MMSs independent of MRI scanners by simulations and experiments. We begin with a brief theory on magnetic forces on superparamagnetic particles in the next section. In subsequent sections, we characterize and simulate the magnetic field generated by an HTS pellet in a uniform field. We then experimentally validate the simulations by showing that the navigation of MMSs in one bifurcation is possible with the HTS pellet. Finally, we calculate the magnetic forces generated by a large HTS pellet and compare with those obtained with DFN.

2. Theory of magnetic forces on superparamagnetic particles

The magnetic force generated on a particle of magnetic moment $\mathbf{m_p} = \mathbf{M_p} V_p$ with a magnetization $\mathbf{M_p}$ and volume V_p in a magnetic field $\mathbf{B}$ is given by:

$$\mathbf{F_p} = \nabla (\mathbf{m_p} \cdot \mathbf{B}) = |\mathbf{M_p}| V_p \nabla |\mathbf{B}|. \quad (1)$$

The last equivalence is true in the case of superparamagnetic particles whose magnetic moment is always parallel to the external field. The magnitude of the force is therefore proportional to the magnetization and volume of the particle and

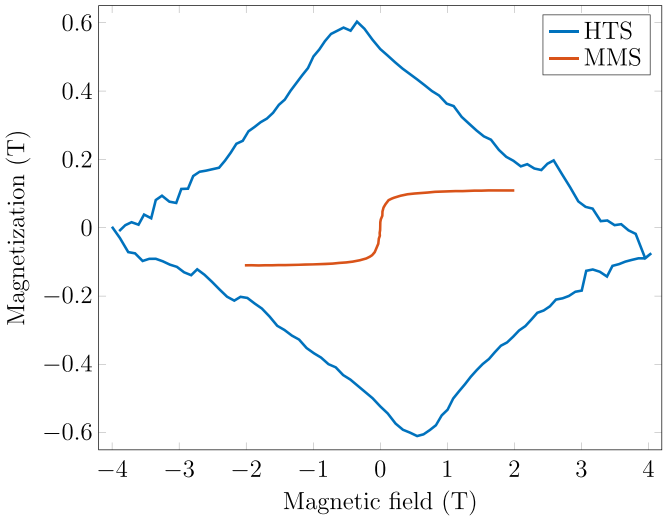

Figure 1. Magnetic hysteresis curves of a 14 × 6 mm $YBa_2Cu_3O_{7-x}$ pellet and MMSs used in this work. The $YBa_2Cu_3O_{7-x}$ hysteresis was measured using a custom magnetometer developed in [31] , while the MMS data was obtained from [9].

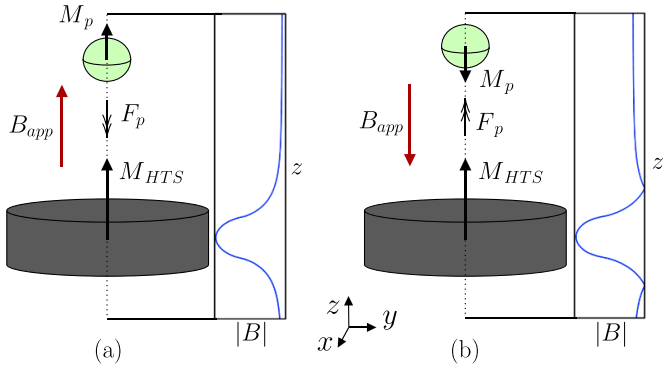

Figure 2. Illustration of the pushing and pulling forces possible with HTS (or PM) bulks in a small uniform field. (a) If the applied field B_{app} is in the same direction as the bulk's magnetization M_{HTS}, the MMSs (green) are attracted to the bulk (gray). (b) If B_{app} is in the opposite direction of M_{HTS}, the MMSs are repelled from the bulk. The norm of the magnetic field along the central axis of the HTS is shown beside each diagram. The size of the MMSs is exaggerated for visualization purposes.

to the external magnetic field gradient. However, $\mathbf{M_p}$ and V are limited by the fact that the particles are generally made of iron oxide embedded in a biodegradable matrix with a maximum diameter of ∼250 μm for liver embolization [22]. The strength of the magnetic force is therefore mainly controlled by the external magnetic field gradient and the magnetic field strength used to magnetize the particles. The direction of the force is purely dependent on the gradient of the norm of the external magnetic field.

Although the magnetic force strongly depends on the MMS properties, it was determined that a gradient of 400 mT/m was sufficient for navigating magnetically saturated MMSs in the vascular network of the human body [21]. For MMSs of 250 μm diameter loaded at 50 weight% with Fe_3O_4 nanoparticles, the saturation magnetization occurs at $\gtrsim$500 mT, as shown in figure 1 [9]. For the MMSs given in figure 1, a gradient of 400 mT/m corresponds to a force of ∼287 nN. Thus, target forces of $F_T = 287$ nN will be aimed at in the next sections.

For HTS bulks, the magnetization decreases as a function of the applied field, as shown in figure 1. Since the magnetic field gradient produced by a magnetized sample is approximately proportional to its magnetic moment, the magnetic force generated by an HTS pellet is maximized at low field values. Therefore, due to their high trapped field potential, HTS bulks can potentially generate stronger remote forces than other proposed methods by increasing the magnetic field gradient surrounding the MMSs instead of the background field strength.

The direction of the remote forces is also an important aspect of MDD systems in order to be able to navigate MMSs in all possible directions. The remnant magnetization of HTS bulks (or PMs) is therefore an advantage since it enables them to either push or pull the superparamagnetic MMSs when inserted in a small uniform field. Figure 2 illustrates this concept, where an HTS bulk of magnetization M_{HTS} is inserted in a small applied field B_{app}. In figure 2(a), M_{HTS} and B_{app} are in the same direction. The norm of the total field $|B|$ along the central axis therefore decreases from the center of the HTS as a function of z. For a MMS above the HTS, a force in the $-z$ direction emerges because $\partial|B|/\partial z < 0$. Thus, when the applied field is in the same direction as the HTS's magnetization, the MMSs are always attracted to the bulk along the central axis.

On the other hand, as seen in figure 2(b), the force between the HTS and the MMSs is repulsive when B_{app} and M_{HTS} are in opposite directions. Indeed, $|B|$ decreases from the center of the HTS until B changes sign due to the applied field in the $-z$ direction. At a certain distance from the HTS, $|B|$ reaches zero and starts increasing as a function of z, such that $\partial|B|/\partial z > 0$ and a repulsive force is felt by the MMS. Hence, not only is it possible to increase the strength of the remote forces using the strong magnetization of HTS bulks, but the direction of the force can also be easily changed with an appropriate applied field. This work therefore seeks to evaluate the above claims both numerically and experimentally.

3. HTS bulk characterization and simulation

In order to determine the potential forces generated by an HTS bulk in a uniform field, we first measured the magnetic field above a 14 mm diameter and 6 mm thick $YBa_2Cu_3O_{7-x}$ bulk using a stack of five THS-119 Hall sensors, as shown in figure 3(a). The z-direction of the field was measured along the central axis of the bulk at 0.6 mm, 4.6 mm, 8.6 mm, 12.6 mm and 16.6 mm from its surface. The pellet was FC magnetized under 3 T, down to 77 K. Figure 3(b) shows the field strength generated by the bulk $B_{HTS} = B - B_{app}$ as a function of the applied field B_{app}. As expected, the curves follow similar behavior to the magnetization curve of figure 1: the magnetic field is strongest near −20 mT due to the high critical current density at low fields combined with the reversible magnetization contribution. The field strength decreases at higher applied fields and at larger distances.

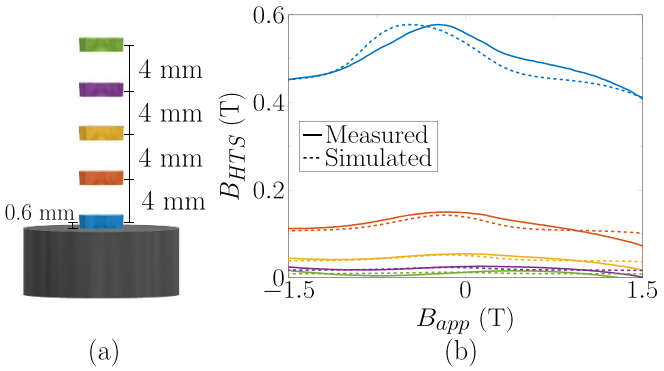

Figure 3. Magnetic field measured above the HTS pellet as a function of the applied field. (a) Position of the five Hall probes used to measure the field. The distance of the active area of the Hall probe from the surface of the bulk is also shown. (b) Comparison of the magnetic field produced by the HTS as a function of the magnetic field and position obtained from the Hall probes and from simulations.

We calculate the magnetic field surrounding the HTS bulk by using Finite Element Method (FEM) simulations. The underlying equations are derived from the H-ϕ formulation [32]:

$$\begin{aligned} &\text{In } \Omega_{nc}: && \nabla \cdot \nabla\phi = 0, \\ &\text{In } \Omega_{c}: && \nabla \times (\rho \nabla \times \mathbf{H}) = -\mu_0 \frac{\mathrm{d}\mathbf{H}}{\mathrm{d}t}, \end{aligned} \tag{2}$$

where the magnetic scalar potential ϕ is defined in non-conducting domains Ω_{nc} as $\mathbf{H} = -\nabla\phi$. The resistivity ρ in the superconducting domain Ω_c is modeled according to the power law model [33]:

$$\rho = \frac{E_{\mathrm{c}}}{J_{\mathrm{c}}} \left(\frac{|\mathbf{J}|}{J_{\mathrm{c}}} \right)^{n-1}, \tag{3}$$

where $\mathbf{J}$ and J_{c} are the current density and critical current density, respectively. The electric field criterion is defined as $E_{\mathrm{c}} = 1\,\mu\mathrm{V\,cm^{-1}}$ and n is the power law exponent. From magnetic relaxation measurements using the Hall sensors [34], we found that $n = 24.7$, in agreement with n values found for other HTS bulks [35–37].

In order to accurately model the magnetic properties of the HTS bulk, we use the field-dependent critical current density measured on small sub-specimens by CAN superconductors on a similarly grown $YBa_2Cu_3O_{7-x}$ bulk [38]. As done in [39], the average J_{c} is taken over all measured sub-specimen in order to obtain the global J_{c} of our pellet as a function of the magnetic field. The FC magnetization was then simulated and the magnetic field generated by the bulk was calculated at the positions of each Hall sensor's active regions. A comparison of the measured and simulated results is shown in figure 3(b), showing good agreement between the two. Consequently, using the magnetization curve of the MMSs in figure 1 and considering MMSs of 239 μm in diameter, the magnetic field obtained by simulations can be used to predict the force generated by the HTS pellet on the MMSs with (1).

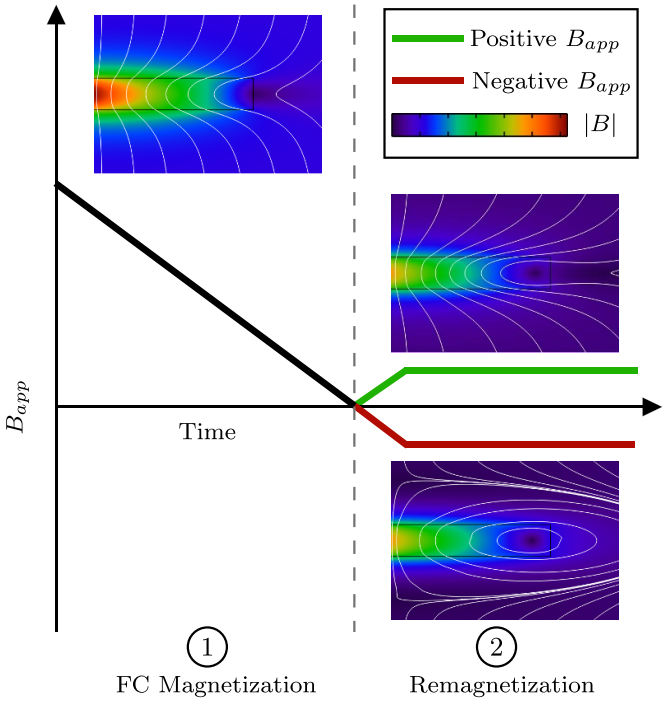

Figure 4. Magnetic field ramp used in the simulations and experiments of this work. The field produced by the HTS bulk at specific applied fields is also shown. The white streamlines represent lines of constant magnetic vector potential.

According to figure 1, the magnetic field gradient produced by the HTS pellet is maximized at low fields. However, the field strength rapidly decreases as a function of distance from the bulk surface, meaning that MMSs far from the bulk are not adequately magnetized. Thus, in order to increase the magnetization of the MMSs, we remagnetize the HTS bulk in a small field, as shown in figure 4. The pellet is first FC magnetized in a field of 2 T, then a small field is applied either parallel or antiparallel to the initial applied field. The magnetic field surrounding the HTS bulk is drastically different depending on the direction of the remagnetizing field, which results in different field gradients.

The remote forces on MMSs surrounding a magnetized HTS bulk in different remagnetizing fields is shown in figure 5. We refer to a positive applied field as a field in the same direction as the HTS's magnetization, while a negative field refers to a field antiparallel to M_{HTS}. As seen in figures 5(a) and (c), where B_{app} is 20 mT and −20 mT, respectively, the direction of the remote forces is inverted at appreciable distance from the sample. F_{T} is achieved at a distance of ∼1.46 cm from the surface of the bulk along the central axis for $B_{\mathrm{app}} = 20$ mT, while it is only at 1.2 cm for $B_{\mathrm{app}} = -20$ mT. The range of F_T increases for applied fields of 50 mT and −50 mT, as seen in figures 5(b) and (d), respectively. Indeed, at 50 mT, the range of F_{T} increases by ∼3 mm, while it increases by ∼5.5 mm at −50 mT along the central axis. Although the direction of the remote forces greatly varies depending on the direction of the applied field and location of the MMSs, we will focus on the central axis above the HTS in the current and following sections for simplicity. On this axis, the forces are either

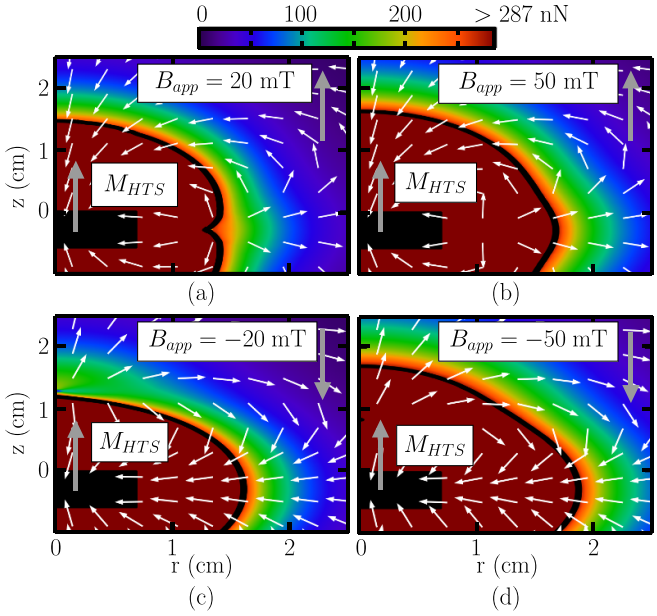

Figure 5. 2D axisymmetric magnetic forces simulated around an HTS pellet magnetized at 2 T in a uniform applied field. The pellet is in a field of (a) 20 mT and (b) 50 mT parallel to its magnetization in the first row, while it is in a field of (c) 20 mT and (d) 50 mT antiparallel to its magnetization in the bottom row. The colors and white arrows represent the norm and direction of the magnetic force, respectively. The black contours show the regions where the target force of 287 nN is achieved. The colorbar maximum has been adjusted to the amplitude of the target force.

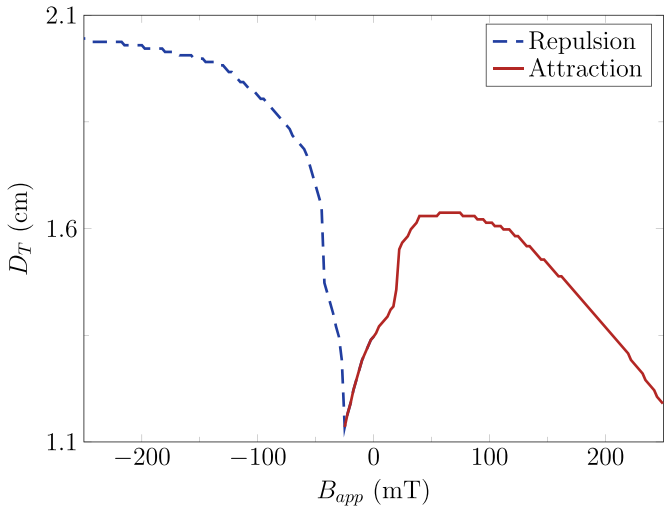

Figure 6. Distance above the surface of the HTS pellet for which the target force is attained along the central axis of the bulk as a function of the applied field. Depending on the applied field, the MMSs are either attracted or repulsed by the pellet, as portrayed by the line color.

attractive (towards the HTS in the $-z$ direction) or repulsive (away from the HTS in the $+z$ direction). An analysis of the whole 3D space surrounding the HTS is given in section 5.

Figure 6 shows the distance D_T above the surface of the bulk for which F_T is achieved as a function of the applied field for the HTS bulk. Many interesting features can be extracted from this figure. Firstly, the attractive force reaches a maximum for an applied field of ∼65 mT. For applied fields higher than 65 mT, the range of the target force decreases, most likely due to a reduction of the HTS bulk's magnetization, leading to smaller field gradients. The optimal distance for an attractive force using the 14×6 mm pellet is therefore at ∼1.65 cm in an applied field of 65 mT.

For negative applied fields, the target force is attractive below −26.5 mT. This can be explained by the fact that at small negative fields, the gradient is only strong near the HTS bulk, where the force is attractive, as seen in figure 2. The behavior of the repulsive force is quite different from the attractive force due to the asymmetric nature of the magnetic hysteresis of the bulk, illustrated in figure 1. Indeed, the magnetization of the bulk increases for relatively small negative applied fields. The value of D_T therefore increases up to a field as high as −250 mT, reaching 2 cm for the small HTS pellet. Note that the smallest D_T does not occur at zero applied fields as naively expected, but at −26.5 mT. This can be explained by the fact that at low negative background fields, the field generated by the bulk is suppressed, leading to a lower MMS magnetization and decreased magnetic force.

The advantage of the applied field is clear from figure 6: with no B_{app}, only an attractive force is possible at a distance of ∼1.35 cm from the surface of the bulk. By inserting the HTS bulk in a relatively small uniform field, the distance for which the target force is achieved is increased and it gives more degrees of freedom depending on the direction of the applied field. Although the D_T achieved here with the 14×6 mm pellet is insufficient for deep tissue navigation, a larger pellet magnetized at stronger fields and lower temperatures could yield stronger forces, as investigated in section 5. In addition, the critical current density could also be increased to achieve stronger forces. In the next section, we evaluate the results established above experimentally.

4. Experimental setup and results

A 14 mm diameter and 6 mm thick $YBa_2Cu_3O_{7-x}$ pellet was prepared by CAN superconductors using the top seeded melt growth technique [38]. The pellet was cooled with liquid nitrogen in a custom-made vacuum insulated stainless steel cryostat. Both the magnetizing and remagnetizing fields were generated with our custom 5 T split-pair electromagnet (American Magnetics Inc.) with a 7.62 cm diameter vertical bore and a 5.08 cm diameter horizontal bore, shown in figure 7.

The MMSs used in this paper were made using the co-precipitation method in order to obtain MMSs of biocompatible sizes and composition for liver embolization [9]. The MMSs were composed of Fe_3O_4 nanoparticles of 12 ± 4 nm diameter coated in C_{12}-bisphosphonate and embedded in a matrix of PLGA. Only 50% of the weight of the MMSs was loaded with Fe_3O_4 nanoparticles in order to accommodate the chemotherapeutic drugs, although these were not added in this work for convenience and cost purposes. The diameter of the MMSs used in this work was measured at $239 \pm 30\,\mu$m. Although the *B*–*H* curve was not measured for the specific

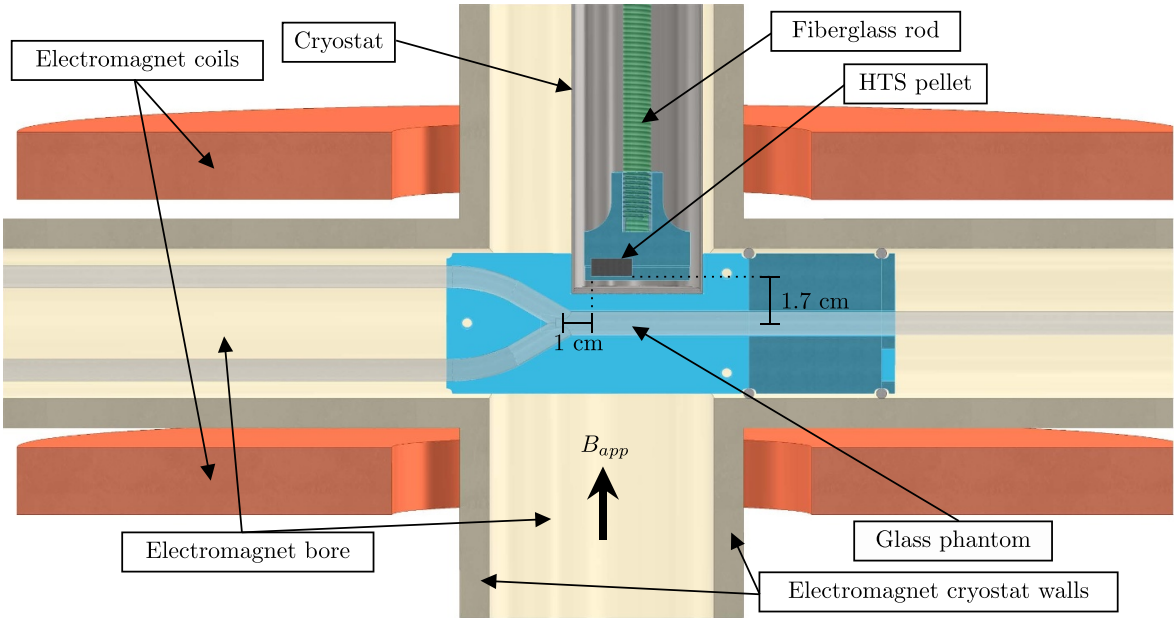

Figure 7. Cross-section of the magnetic part of the experimental setup consisting of the HTS bulk, the electromagnet coils and glass phantom. The blue parts are made from 3D-printed PLA.

MMSs used in this study, the preparation method and diameter are nearly identical to the MMSs measured in [9], so that the *B*–*H* curve of figure 1 remains valid.

A custom glass phantom (fabricated by Cédric Ginart Glass in Montreal, Canada) was made to replicate the main branch of the hepatic arterial tree (4 mm and 3 mm inner diameter in the main and sub-branches, respectively). A cross sectional view of the experimental setup used to navigate MMSs in a glass bifurcation is shown in figure 7. The glass phantom, HTS pellet and cryostat were fixed in the electromagnet bore using 3D-printed PLA (polylactic acid) parts such that the HTS pellet and glass bifurcation were in the uniform field region of the electromagnet. The pellet was positioned at a horizontal distance of ∼10 mm from the bifurcation in order to generate enough force on the MMSs before they enter the bifurcation, as done in [25]. The vertical distance between the centerline of the glass phantom and the HTS pellet was set at 1.7 cm, which is around the maximum D_T found for the attractive force in figure 6. The top of the bifurcation is in the positive B_{app} direction.

A pulsatile flow of water at 60 cycles per minute and 30% systole was pumped in the glass phantom using a 1421 Harvard Apparatus pulsatile heart pump to mimic blood flow and help reduce friction of the MMSs on the glass walls [40]. A schematic diagram of the complete navigation setup is shown in figure 8. A bypass flow was imposed at the output of the blood pump in order to reduce the flow in the main branch and get rid of any bubbles. The MMSs were injected using a 5 F catheter (Cobra 2 Glidecath) attached to a syringe. A $Nd_2Fe_{14}B$ PM was attached at each exit of the bifurcation outside the electromagnet in order to trap the MMSs for counting purposes. Finally, valves were attached at the ends of the bifurcation in order to set an equal flow in each branch.

After each navigation, the MMSs were collected on Stonylab filter papers. Photos of the MMSs were captured and used to automatically count the number of MMSs in each branch using the open-source software ImageJ [41].

The HTS bulk was FC magnetized at 2 T with a ramp rate of 2.2 mT s^{-1}. In all tests, the magnetizing field was ramped down to zero before ramping up to the desired remagnetizing field. A magnetic relaxation time of at least ∼20 min was imposed before each set of measurements in order to prevent flux creep effects [42].

An arbitrary number of MMSs ranging from $177 - 862$ was manually injected with a syringe. The experiments were therefore repeated five times for fields lower than 50 mT and three times for higher fields to reduce effects caused by different MMS numbers. We found that at background fields higher than 50 mT, the MMSs got trapped in the non-uniform field of the electromagnet (after the bifurcation), so that the field had to be ramped down to zero after each experiment. However, this would not occur in a human-sized electromagnet that would be used in a clinical setting, as discussed below. The FC magnetization process was therefore repeated before each measurement above ±50 mT.

The flow of water was kept at 1.2 ± 0.1 ml s^{-1} in the main branch of the glass bifurcation. This is slower than *in-vivo* measurements of the blood flow in the hepatic artery [43], but in practice, this flow can be reduced to as low as 0.3 ml s^{-1} using a balloon catheter [22].

The percentage of MMSs navigated in the top branch of the glass bifurcation as a function of the background magnetic field is shown in figure 9. Without the HTS, around 19% of the MMSs reached the top branch irrespective of the applied field. The majority of MMSs reach the bottom branch due to

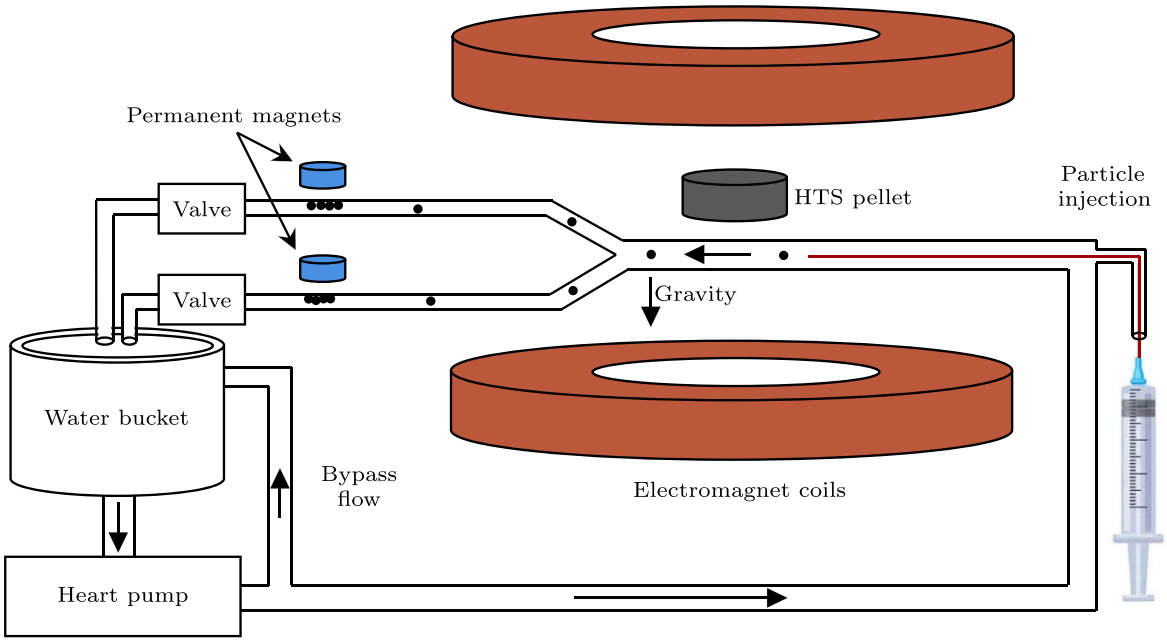

Figure 8. Schematic diagram of the *in-vitro* setup used for the navigation.

the gravitational force given by:

$$F_g = V_p\,(\rho_p - \rho_w)\,g \approx 137\ \text{nN}, \tag{4}$$

where V_p is the volume of MMSs, ρ_p is the MMS density of 2.95 g/cm^3, ρ_w is the water density of 0.998 g/cm^3 and g is the acceleration due to gravity [44]. A small fraction of MMSs still reaches the top branch due to phenomena such as turbulence, irregularities in the glass phantom and the orientation of the catheter at the injection site. Note that the data without the HTS has only been measured for positive applied fields and is therefore mirrored around $B_{\text{app}} = 0$ T. This is valid because the field is symmetric without the HTS bulk.

As explained in the last section, in zero or positive background fields, the MMSs are attracted towards the HTS. This effect can be seen in figure 9, where the percentage of MMSs reaching the top branch is increased compared to the navigation without HTS. With no applied field, 44% of MMSs are navigated upwards, while this efficiency is increased to 83% with a field of only 50 mT. At 200 mT, the navigation efficiency is lower than at 50 mT, as expected from the reduction of the remote force at large positive fields predicted by the simulations (see figure 6).

Interestingly, merely ∼5% of the MMSs reach the top branch at −200 mT. This could be explained by the fact that the HTS pushes the MMSs away, so that both the gravitational and magnetic forces are directed downwards. The magnetic force increases from −50 mT to −200 mT, as expected by the simulations and explained in the last section.

Although many phenomena such as gravity, drag forces and turbulence have been neglected in the simulations, the results obtained in figure 6 qualitatively follow the navigation success of figure 9. In both cases, the y-axis data increases for small positive applied fields and falls off for larger applied fields. The D_{T} predicted in figure 6 shows that the force increases for negative applied fields down to −250 mT, which is what is observed in figure 9 since less and less MMSs reach the top branch as a function of the applied field.

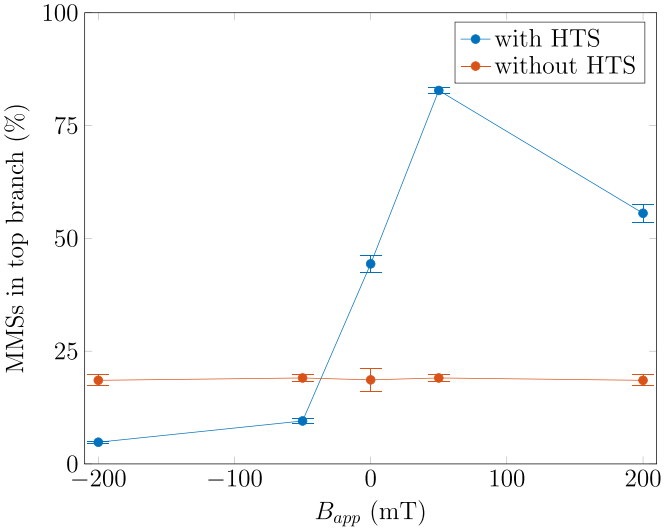

Figure 9. Percentage of MMSs navigated in the top branch of the glass phantom as a function of the applied field with and without the HTS pellet.

In figure 10, we show the navigation efficiency of the HTS pellet in a field of 50 mT as a function of its distance from the bifurcation. The navigation efficiency decreases approximately exponentially as a function of distance since the magnetic field (or field gradient) generated by the HTS rapidly decreases

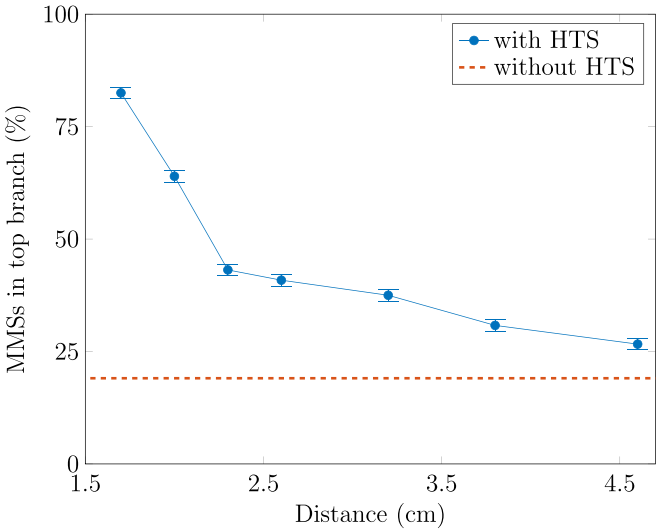

Figure 10. Percentage of MMSs navigated in the top branch of the glass phantom as a function of the distance between the surface of the HTS pellet and the centerline of the bifurcation. The error bars represent the maximum error obtained in figure 9.

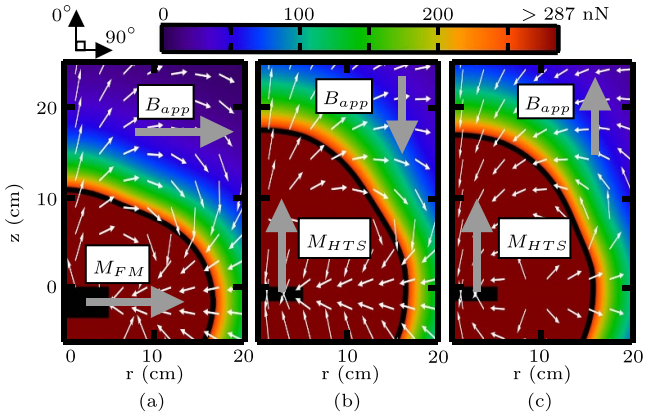

Figure 11. Remote magnetic forces generated around (a) a low carbon steel cylinder in a 3 T uniform field, (b) a $GdBa_2Cu_3O_{7-x}$ bulk magnetized at 5 T and inserted in a uniform field of −250 mT, and (c) a $GdBa_2Cu_3O_{7-x}$ bulk magnetized at 5 T and inserted in a uniform field of 250 mT.

from its surface, as seen in figure 3. At >4.5 cm, the fraction of MMSs reaching the top bifurcation approaches that obtained without the HTS.

5. Potential forces produced by a large HTS bulk

The small pellet used in the previous sections yielded target forces at distances of $1.5-2$ cm. However, for successful deep tissue navigation, the target forces need to be achieved at distances of at least 10 cm from the surface of the patient. This can be accomplished in DFN, where a soft FM core of sufficient size is inserted in the strong uniform field of an MRI. However, the forces generated in deep tissues is lacking for complex routes in the vascular network using this method, since the direction of the force must drastically vary over short distances [26]. In this section, we therefore compare the forces generated by a soft FM core in a strong uniform field to the ones produced by a large magnetized HTS bulk in a much weaker uniform field in order to evaluate the potential of the approach investigated above. As opposed to the last section, we focus herein on the forces obtained in the whole 3D space surrounding the HTS/FM in order to evaluate the potential of each in achieving forces in all spatial directions.

Latulippe *et al* found that the ideal FM core to insert inside an MRI with reasonable insertion force is a low carbon steel 1020 cylinder of 108 mm diameter and 33.6 mm thickness [27]. The resulting magnetic forces generated on the MMSs around the ferromagnet in the 3 T uniform field of the MRI scanner is shown in figure 11(a). Note that in this case, the field is along the easy axis of the ferromagnet in order to eliminate torque. In addition, the magnetization is always in the same direction of the applied field since a soft ferromagnet is used. The target force is obtained at >10 cm for forces parallel to the central axis of the pellet, but the distance quickly drops for forces in other directions.

The magnetic force generated by the HTS bulk of the previous sections can be increased in two ways: by magnetizing the pellet at higher fields and by using a larger pellet such that the magnetic moment and resulting field gradients are stronger. The largest commercially available single grain HTS bulk is a $GdBa_2Cu_3O_{7-x}$ pellet of 100 mm diameter and 15 mm thickness [45], so we will use these dimensions for the following analysis. We use the field-dependent critical current density at 70 K measured by Can superconductors on a similarly grown sample. Superconducting quantum interference device measurements were taken on a small sample below the seed surface, so the global $J_c(H)$ of the large HTS pellet is overestimated in this case. However, the operating temperature could be lowered in order to obtain similar $J_c(H)$ values.

Although the strongest trapped field in $GdBa_2Cu_3O_{7-x}$ bulks is 17.6 T [46], this value is currently impractical for real-world applications and especially for large samples. In 2007, Sakai *et al* managed to magnetize a 140 mm diameter bulk in a field of 4 T at 65 K [47]. We therefore use a magnetizing field of 5 T to trap field in the 100 × 15 mm bulk in our simulations. The magnetic forces could be further increased by using a 140 mm diameter bulk, but using a similar diameter between the HTS and the ferromagnet used for DFN leads to a fairer comparison, even though the thickness of the ferromagnet is slightly larger than that of the HTS.

Following the procedure of section 3, we find the background field for which the maximum amount of force is generated around the HTS by calculating D_T along its central axis as a function of the applied field. As shown in figure 12, the distance is maximized for an attractive force at an applied field of ∼250 mT, while it is maximized for a repulsive force at $B_{app} < -1$ T. Note that the behavior of D_T for the 100 × 15 mm pellet is very similar to the 14 × 6 mm pellet of figure 6, although the range of the target force is increased by a factor of nearly ten. We again find the dip in D_T at small negative values of B_{app}.

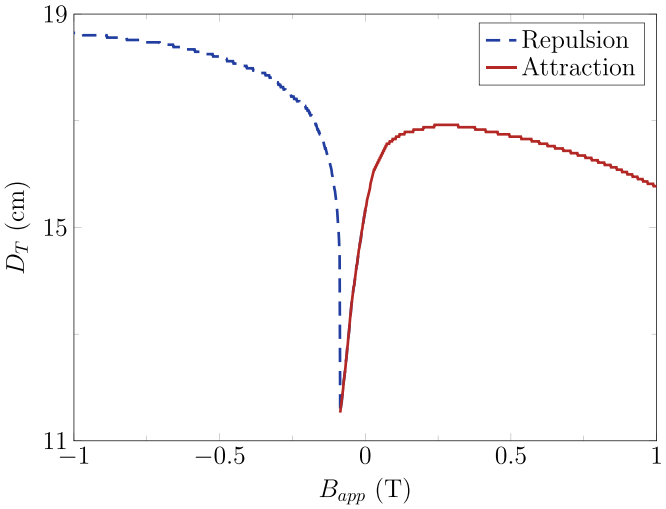

Figure 12. Distance for which the target force is obtained along the central axis of a 100 mm diameter and 15 mm thick $GdBa_2Cu_3O_{7-x}$ bulk magnetized at 5 T as a function of the applied field.

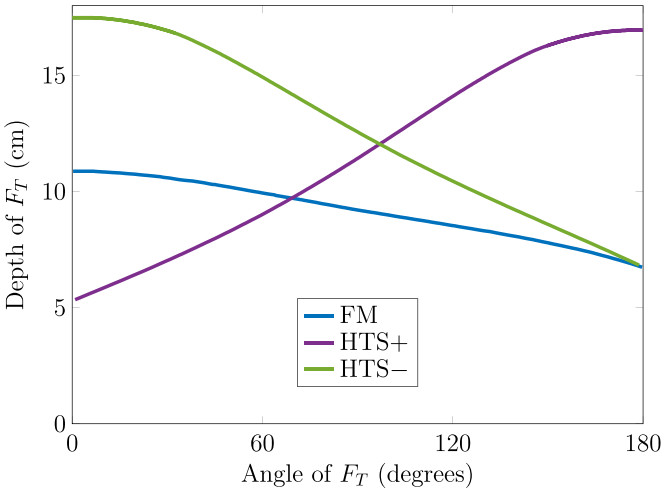

Figure 13. Depth of the target force obtained as a function of its angle along the black contours in figure 11. FM represents the force obtained by the ferromagnetic core, while HTS+ and HTS− represent the forces generated by the HTS pellet in a background field of +250 mT and −250 mT, respectively.

Figures 11(b) and (c) show the remote forces surrounding the HTS bulk for applied fields of −250 mT and 250 mT, respectively. Compared to the FM sample of figure 11(a), we find that the target force's range is greater in the HTS case. In addition, the direction of the remote forces surrounding the HTS bulk is more diverse than in the FM case due to the different directions resulting from either a positive or negative applied field. This directional change emerges only due to the remnant field of the HTS, so it would not be possible using the soft FM cores required in DFN. It's important to mention that the HTS needs to be cooled in a cryostat, such that the cryostat thickness must be considered when comparing both materials. However, vacuum sealed cryostats can be made with millimeter-sized thicknesses, so that this will be neglected in the comparison.

In order to obtain an MDD system capable of navigating MMSs in deep tissues, the target force must be obtained at distances of >10 cm from the patient surface and in all spatial directions. Consequently, we compare the depth of the target force achieved by the FM and HTS pellets as a function of the angle of the force in figure 13. This figure follows the black contours of figure 11 and maps the z depth as a function of the angle of the target force. An angle of 0° (180°) represents a force in the $+z$ ($-z$) direction. In the FM case, deep tissue navigation (>10 cm) is possible if the required force direction is less than ∼ 60°, but the range of the force quickly drops for larger angles. Indeed, for attractive forces (180°), the depth of the target force is only 6.7 cm. This can be overcome by using multiple FM cores, but the forces generated are still limited for complex bifurcations [26]. Note that the trajectory of the MMSs is not taken into account in any of the results shown in this work. It is assumed that the MMSs are moving in arbitrary directions and that the magnetic forces will redirect their trajectory.

The HTS bulk in a negative applied field shows similar behavior to the FM pellet, but at larger distances from the surface of the bulk. Indeed, for a force at 0°, the range of the target force is increased by nearly 7 cm with the HTS. This enhancement drops for larger angles; both the HTS and FM generate nearly identical forces at angles near 180°.

Inserting the HTS in a positive applied field yields complementary forces to the negative field case. For $B_{app} = 250$ mT, the strongest force is achieved at an angle of 180°. The depth achieved at 180° is increased by more than 10 cm compared to the FM and HTS in a negative field. This depth decreases with the force angle, reaching only 5.3 cm for an angle of 0°.

Figure 13 shows the clear advantage of using an HTS as opposed to a FM. The HTS remagnetized in a negative applied field produces stronger forces than in DFN for all force angles. The forces can also be supplemented by considering a positive remagnetizing field, such that the target force can be obtained at depths of over 12 cm for all force directions in 3D space. We find that for an angle of 97°, both HTS remagnetized in a positive or negative field yield the same target force depth. For lower angles, it is best to remagnetize the HTS in a negative field, while for larger angles a positive remagnetizing field yields a larger depth of F_T.

6. Discussion

We have shown that plunging a magnetized HTS bulk in a relatively low background field can both increase the magnetic forces exerted on small, magnetized particles and enable more directional changes of these forces. In addition, the forces produced by the HTS bulks in our simulations were significantly higher than those obtained using FMs for all directions. However, it is not yet clear how these forces can be made to vary rapidly for multi-bifurcation navigation. In DFN, multiple FM cores are carefully placed in close proximity to each other to appropriately distort the uniform field of an MRI scanner. This could also be used for HTS bulks, but it is unclear how several HTS bulks interact in close proximity. Recently,

Houbart *et al* have studied the interaction between HTS bulks in a Halbach array [48–50], but a study specific to MDD is needed. A single HTS bulk could also be used by moving it around the patient's body with a robotic arm [13] and possibly changing the sign of the applied field such that rapid changes in field gradients are produced.

In all cases, a better cryogenic system is needed in order to cool the pellet in all 360° orientations. Liquid nitrogen was used in this work for simplicity, but this constrained the pellet to be vertically inserted into the electromagnet so as to not spill the cryogenic liquid. Depending on the operating temperatures required, cryogenic nitrogen or helium gas (instead of liquid) could be used for cooling in other orientations. In any case, the temperature must be kept well below the critical temperature to obtain a sufficiently high critical current density and the thermal stability must be reasonable to reduce flux creep. In addition, the bulks could also be further cooled after the magnetization to minimize the effects of flux creep even more.

The need for a relatively small uniform field of 250 mT required with the HTS bulks is interesting for reducing the cost of applying this technology in comparison with the $1.5-3$ T needed for MRN and DFN, and therefore makes the treatment more widely accessible. A field of ~ 5 T is still required for magnetizing the HTS bulks, but the volume of the uniform field would be small and could possibly be done at relatively low cost using copper coils with pulsed field magnetization [35, 51–54]. The complete envisioned MDD system using HTS bulks is shown in figure 14. A large Helmholtz coil pair could be used to generate the weak, uniform field in the region of interest inside the patient, while a compact Helmholtz coil pair could be used to highly magnetize the HTS bulks before being positioned near the patient. The need for a weak field could potentially give more space for clinical manipulations near the patient than other proposed MDD methods using MRI scanners.

Another question that remains is how the navigation efficiency will be determined when using HTS bulks. In DFN and MRN, the imaging of the MMSs can be done with the use of MRI technology at $1.5-3$ T. However, in this work, we found that low background fields are required for generating the maximum amount of remote forces with HTS bulks. This low background field requirement would lead to a lower resolution in the MRI imaging, but recent progress in MRI technology has made low-field ($\sim$200 mT) imaging achievable with advances in radio-frequency coils, powered gradients, optimized pulse sequences and deep learning noise subtraction [55]. The imaging could therefore possibly be done with MRI technology at $\sim$250 mT, which might be sufficient to accurately track the MMSs. However, with the system proposed in figure 14, a more sophisticated full-body electromagnet would be required to generate a more uniform field for MRI imaging. Other imaging avenues include using x-ray or ultrasound probes [3, 13].

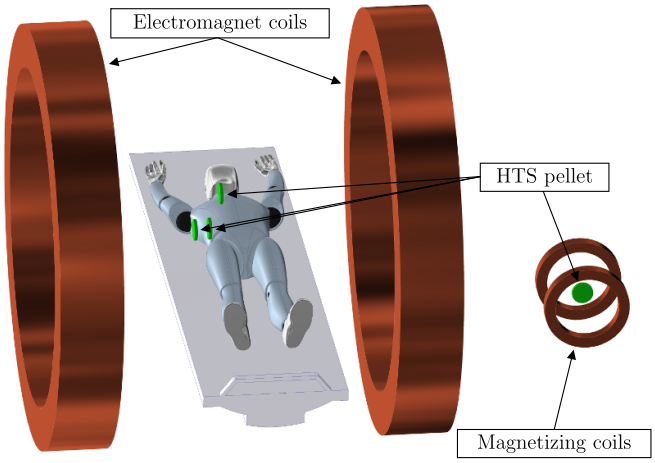

Figure 14. Envisioned MDD system using HTS bulks. A large split-pair electromagnet could be used to generate a weak, uniform field at the region of interest inside the patient, while a small electromagnet could be used to highly magnetize the HTS bulks. As done in DFN, several bulks could be used to generate the rapid directional changes in field gradients.

7. Conclusion

In this work, we investigated the remote magnetic forces generated by a magnetized HTS bulk in a uniform field on superparamagnetic MMSs. We first characterized a 14×6 mm $YBa_2Cu_3O_{7-x}$ pellet using a stack of Hall probes above the sample surface and showed that FEM simulations were in agreement with the magnetic field measurements. The magnetic forces generated by the HTS on the MMSs were calculated as a function of the applied field, showing that either attractive or repulsive forces can be obtained depending on the direction of the applied field with respect to the HTS's magnetization. We found that for the 14×6 mm HTS magnetized at 2 T, the maximum attractive force occurs at an applied field of $\sim$65 mT, while the repulsive force is maximized for fields lower than -250 mT.

In order to evaluate the simulation results, we constructed an experimental setup mimicking the hepatic artery of a human liver. MMSs were injected in a glass bifurcation and navigated to each branch using a magnetized HTS bulk in a uniform field. By counting the number of MMSs reaching the top branch of the bifurcation, we found that the attractive force of the HTS is maximized at $\sim$ 50 mT, while the repulsive force is at a maximum for the lowest applied field value of -200 mT observed, confirming the simulation results. We also found that the navigation efficiency drops exponentially as the distance between the HTS and the glass bifurcation is increased.

Finally, we compared the magnetic forces generated between a FM and an HTS by simulation. A 100 mm diameter and 15 mm thick HTS bulk magnetized at 5 T was considered and compared with a FM of similar dimensions. The FM was

inserted in a uniform field of 3 T as is done in DFN, while the optimal background field for the HTS case was found to be ±250 mT. We found that the HTS produced stronger forces with more DOFs than the FM. Indeed, the target force was found to be achieved in all directions for deep tissue distances (>10 cm) with the HTS, while the FM was found to lack in force strength for forces at angles greater than 60°.

Though many questions remain to be answered before a usable MDD system can be achieved using HTS bulks, this work paves the way for future research avenues. A method for generating rapid directional changes in the magnetic field gradient and more sophisticated cryogenic systems are needed for multi-bifurcation navigation. Furthermore, an imaging modality compatible with low-field navigation must be developed in order to evaluate the navigation efficiency.

Data availability statement

The data cannot be made publicly available upon publication because they are not available in a format that is sufficiently accessible or reusable by other researchers. The data that support the findings of this study are available upon reasonable request from the authors.

Acknowledgments

This work was supported in part by the Fonds de recherche du Québec—Nature et Technologies (FRQNT), TransMedTech Institute and its main funding partner, the Canada First Research Excellence Fund.

ORCID iD

Alexandre Arsenault https://orcid.org/0000-0003-2758-9495

References

[1] Felfoul O *et al* 2018 *Med. Sci.* **34** 197–9
[2] Wilson W R and Hay M P 2011 *Nat Rev Cancer* **11** 393–410
[3] Martel S 2014 Advantages and limitations of the various magnetic manipulation methods of untethered agents in the human body *2014 IEEE/ASME Int. Conf. on Advanced Intelligent Mechatronics* (IEEE) pp 13–18
[4] Pitt W G, Husseini G A and Staples B J 2004 *Expert Opin. Drug Deliv.* **1** 37–56
[5] Yan L, Shen J, Wang J, Yang X, Dong S and Lu S 2020 *Dose-Response* **18** 1559325820936161
[6] Starpax Biopharma (available at: https://starpaxbiopharma.com/about/)
[7] Shubayev V I, Pisanic T R and Jin S 2009 *Adv. Drug Deliv. Rev.* **61** 467–77
[8] Mahmoudi M, Shokrgozar M A, Simchi A, Imani M, Milani A S, Stroeve P, Vali H, Häfeli U O and Bonakdar S 2009 *J. Phys. Chem.* C **113** 2322–31
[9] Nosrati Z, Li N, Michaud F, Ranamukhaarachchi S, Karagiozov S, Soulez G, Martel S, Saatchi K and Häfeli U O 2018 *ACS Biomater. Sci. Eng.* **4** 1092–102
[10] Gupta A K and Gupta M 2005 *Biomaterials* **26** 3995–4021
[11] Shevtsov M, Nikolaev B, Marchenko Y, Yakovleva L, Skvortsov N, Mazur A, Tolstoy P, Ryzhov V and Multhoff G 2018 *IJN* **13** 1471–82
[12] Thomas G *et al* 2019 *ACS Omega* **4** 2637–48
[13] Tognarelli S, Castelli V, Ciuti G, Di Natali C, Sinibaldi E, Dario P and Menciassi A 2012 *J. Robot. Surg.* **6** 5–12
[14] Johnson J, Kent T, Koda J, Peterson C, Rudge S and Tapolsky G 2002 *Eur. Cells Mater.* **3** 12–15 (available at: https://www.researchgate.net/publication/237547786_The_MTC_technology_A_platform_technology_for_the_site-specific_delivery_of_pharmaceutical_agents/citations)
[15] Nakagawa K, Mishima F, Akiyama Y and Nishijima S 2012 *IEEE Trans. Appl. Supercond.* **22** 4903804
[16] Nishijima S, Mishima F, Tabata Y, Iseki H, Muragaki Y, Sasaki A and Saho N 2009 *IEEE Trans. Appl. Supercond.* **19** 2257–60
[17] Mathieu J B, Beaudoin G and Martel S 2006 *IEEE Trans. Biomed. Eng.* **53** 292–9
[18] Li N *et al* 2019 *Ann. Biomed. Eng.* **47** 2402–15
[19] Mathieu J B and Martel S 2007 *Biomed. Microdevices* **9** 801–8
[20] Mathieu J B and Martel S 2010 *Magn. Reson. Med.* **63** 1336–45
[21] Pouponneau P, Leroux J C, Soulez G, Gaboury L and Martel S 2011 *Biomaterials* **32** 3481–6
[22] Li N *et al* 2022 *IEEE Trans. Biomed. Eng.* **69** 2616–27
[23] Tous C *et al* 2021 *Ann. Biomed. Eng.* **49** 3724–36
[24] Li N *et al* 2024 *Sci. Robot.* **9** eadh8702
[25] Latulippe M and Martel S 2015 *IEEE Trans. on Robot.* **31** 1353-63
[26] Latulippe M and Martel S 2018 *IEEE Trans. Magn.* **54** 1–12
[27] Latulippe M and Martel S 2017 Seeking optimal magnetic core shapes for strong gradient generation in Dipole Field Navigation *2017 Int. Conf. on Manipulation, Automation and Robotics at Small Scales (MARSS)* pp 1–7
[28] Shi Y, Li N, Tremblay C C and Martel S 2021 *IEEE/ASME Trans. Mechatronics* **26** 214–25
[29] Latulippe M and Martel S 2016 A Progressive Multidimensional Particle Swarm Optimizer for magnetic core placement in Dipole Field Navigation *2016 IEEE/RSJ Int. Conf. on Intelligent Robots and Systems (IROS)* pp 2314–20
[30] Arsenault A and Sirois F Simulation of remote forces generated by high-temperature superconducting bulks for magnetic drug delivery (https://doi.org/10.1109/TASC.2023.3268828)
[31] Arsenault A, Charpentier-Pépin B, Forcier A, Nassiri N, Bellemare J, Lacroix C, Ménard D, Sirois F, Bernier F and Lamarre J 2023 *Rev. Sci. Instrum.* **94** 085116
[32] Arsenault A, Sirois F and Grilli F 2021 *IEEE Trans. Appl. Supercond.* **31** 1–11
[33] Rhyner J 1993 *Physica* C **212** 292–300
[34] Houbart M, Fagnard J F, Dennis A, Namburi D K, Shi Y, Durrell J H and Vanderbemden P 2020 *Supercond. Sci. Technol.* **33** 064003
[35] Ainslie M D, Srpcic J, Zhou D, Fujishiro H, Takahashi K, Cardwell D A and Durrell J H 2018 *IEEE Trans. Appl. Supercond.* **28** 1–7
[36] Takahashi K, Fujishiro H and Ainslie M D 2018 *Supercond. Sci. Technol.* **31** 044005
[37] Zou S, Zermeño V M R and Grilli F 2016 *IEEE Trans. Appl. Supercond.* **26** 1–5
[38] Hlásek T and Plecháček V 2015 *IEEE Trans. Appl. Supercond.* **25** 1–4
[39] Zou J, Ainslie M D, Hu D, Zhai W, Devendra Kumar N, Durrell J H, Shi Y H and Cardwell D A 2015 *Supercond. Sci. Technol.* **28** 035016

[40] Li N, Michaud F, Nosrati Z, Loghin D, Tremblay C, Plantefève R, Saatchi K, Häfeli U O, Martel S and Soulez G 2019 *IEEE Trans. Biomed. Eng.* **66** 2331–40
[41] Rasband W (available at: ImageJ https://imagej.nih.gov/ij/index.html)
[42] Ainslie M and Fujishiro H 2019 *Numerical Modelling of Bulk Superconductor Magnetisation* (IOP Publishing Ltd)
[43] Roldán-Alzate A, Frydrychowicz A, Niespodzany E, Landgraf B R, Johnson K M, Wieben O and Reeder S B 2013 *J. Magn. Reson. Imaging* **37** 1100–8
[44] Li N 2019 *Flow Control and MRI-compatible Particle Injector: Application to Magnetic Resonance Imaging* Ph.D. thesis Polytechnique Montréal (available at: https://publications.polymtl.ca/3878/1/2019_NingLi.pdf)
[45] CAN Superconductors (available at: www.can-superconductors.com/levitation-bulk.html@)
[46] Durrell J H *et al* 2014 *Supercond. Sci. Technol.* **27** 082001
[47] Sakai N, Nariki S, Nagashima K, Miryala M, Murakami M and Hirabayashi I 2007 *Phys* C **305–309** 460–462
[48] Houbart M, Fagnard J F, Dular J, Dennis A R, Namburi D K, Durrell J H, Geuzaine C, Vanderheyden B and Vanderbemden P 2022 *Supercond. Sci. Technol.* **35** 064005
[49] Houbart M, Fagnard J F, Dular J, Dennis A R, Durrell J H, Geuzaine C, Vanderheyden B and Vanderbemden P 2023 *Supercond. Sci. Technol.* **36** 115012
[50] Houbart M, Fagnard J F, Harmeling P, Dular J, Dennis A R, Namburi D K, Durrell J H, Geuzaine C, Vanderheyden B and Vanderbemden P 2024 *Supercond. Sci. Technol.* **37** 095009
[51] Ainslie M D, Fujishiro H, Mochizuki H, Takahashi K, Shi Y H, Namburi D K, Zou J, Zhou D, Dennis A R and Cardwell D A 2016 *Supercond. Sci. Technol.* **29** 074003
[52] Ainslie M D, Zhou D, Fujishiro H, Takahashi K, Shi Y H and Durrell J H 2016 *Supercond. Sci. Technol.* **29** 124004
[53] Fujishiro H, Tateiwa T, Fujiwara A, Oka T and Hayashi H 2006 *Physica C* **334–338** 445–448
[54] Tsui Y, Moseley D A, Dennis A R, Shi Y H, Beck M R, Cientanni V, Cardwell D A, Durrell J H and Ainslie M D 2022 *Supercond. Sci. Technol.* **35** 084004
[55] Hori M, Hagiwara A, Goto M, Wada A and Aoki S 2021 *Invest. Radiol.* **56** 669–79